# Fluid mixing as primary trigger for cassiterite deposition: Evidence from in situ $\delta$18O-$\delta$11B analysis of tourmaline from the world-class San Rafael tin (-copper) deposit, Peru

Matthieu Harlaux, Kalin Kouzmanov, Stefano Gialli, Katharina Marger, Anne-Sophie Bouvier, Lukas Baumgartner, Andrea Rielli, Andrea Dini, Alain Chauvet, Miroslav Kalinaj, et al.

# Fluid mixing as primary trigger for cassiterite deposition: Evidence from in situ $\delta^{18}$O-$\delta^{11}$B analysis of tourmaline from the world-class San Rafael tin (-copper) deposit, Peru

Matthieu Harlaux [a,b,*], Kalin Kouzmanov [a], Stefano Gialli [a], Katharina Marger [c], Anne-Sophie Bouvier [c], Lukas P. Baumgartner [c], Andrea Rielli [d], Andrea Dini [d], Alain Chauvet [e], Miroslav Kalinaj [f], Lluís Fontboté [a]

[a] Department of Earth Sciences, University of Geneva, 1205 Geneva, Switzerland
[b] Nevada Bureau of Mines and Geology, University of Nevada, Reno, NV 89557, USA
[c] Institute of Earth Sciences, University of Lausanne, 1015 Lausanne, Switzerland
[d] Istituto di Geoscienze e Georisorse, CNR, 56124 Pisa, Italy
[e] Géosciences Montpellier, UMR 5243-CNRS, 34095 Montpellier, France
[f] Minsur S.A., Jr. Lorenzo Bernini 149, San Borja, Lima 27, Peru

ARTICLE INFO

*Article history:*
Received 16 November 2020
Received in revised form 7 March 2021
Accepted 11 March 2021
Available online 24 March 2021
Editor: R. Hickey-Vargas

*Keywords:*
tourmaline
oxygen isotopes
boron isotopes
tin deposit
hydrothermal fluids
fluid mixing

ABSTRACT

We present a high-resolution in situ study of oxygen and boron isotopes measured in tourmaline from the world-class San Rafael Sn (–Cu) deposit (Central Andean tin belt, Peru) aiming to trace major fluid processes at the magmatic-hydrothermal transition leading to the precipitation of cassiterite. Our results show that late-magmatic and pre-ore hydrothermal tourmaline has similar values of $\delta^{18}$O (from 10.6‰ to 14.1‰) and $\delta^{11}$B (from −11.5‰ to −6.9‰). The observed $\delta^{18}$O and $\delta^{11}$B variations are dominantly driven by Rayleigh fractionation, reflecting tourmaline crystallization in a continuously evolving magmatic-hydrothermal system. In contrast, syn-ore hydrothermal tourmaline intergrown with cassiterite has lower $\delta^{18}$O values (from 4.9‰ to 10.2‰) and in part higher $\delta^{11}$B values (from −9.9‰ to −5.4‰) than late-magmatic and pre-ore hydrothermal tourmaline, indicating important contribution of meteoric groundwater to the hydrothermal system during ore deposition. Quantitative geochemical modeling demonstrates that the $\delta^{18}$O-$\delta^{11}$B composition of syn-ore tourmaline records variable degrees of mixing of a hot Sn-rich magmatic brine with meteoric waters that partially exchanged with the host rocks. These results provide thus direct in situ isotopic evidence of fluid mixing as a major mechanism triggering cassiterite deposition. Further, this work shows that combined in situ $\delta^{18}$O and $\delta^{11}$B analyses of tourmaline is a powerful approach for understanding fluid processes in dynamic magmatic-hydrothermal environments.

## 1. Introduction

Tin and W mineralization is spatially and genetically associated with reduced granitoids that were generated in orogenic belts by melting of tectonically thickened sedimentary sequences (Romer and Kroner, 2016). Cassiterite ± wolframite-bearing quartz vein systems are a specific type of Sn-W deposits that are emplaced in the upper parts of evolved granitic intrusions or extending into surrounding country rocks (Černý et al., 2005). While the mineralizing fluids and metals are generally interpreted to be of magmatic origin (Audétat et al., 2000a,b; Hulsbosch et al., 2016; Harlaux et al., 2018), the precipitation mechanism(s) of ore minerals remain(s) debated. Cooling, boiling, fluid-rock interaction, and mixing with external fluids have been proposed as major processes controlling cassiterite deposition (Heinrich, 1990). Among these processes, fluid mixing is considered as the most likely effective mechanism based on mineral geochemistry, fluid inclusion, and stable isotope data (Audétat et al., 2000a,b; Vallance et al., 2001; Fekete et al., 2016; Van Daele et al., 2018; Legros et al., 2019; Hong et al., 2020). Korges et al. (2018) challenged this model and suggested depressurization and boiling of magmatic fluid as major factors for Sn-W deposit formation.

In the present paper, we report high-resolution in situ oxygen and boron isotope measurements by secondary ion mass spectrom-

* Corresponding author at: Nevada Bureau of Mines and Geology, University of Nevada, Reno, NV 89557, USA.
*E-mail address:* mharlaux@unr.edu (M. Harlaux).

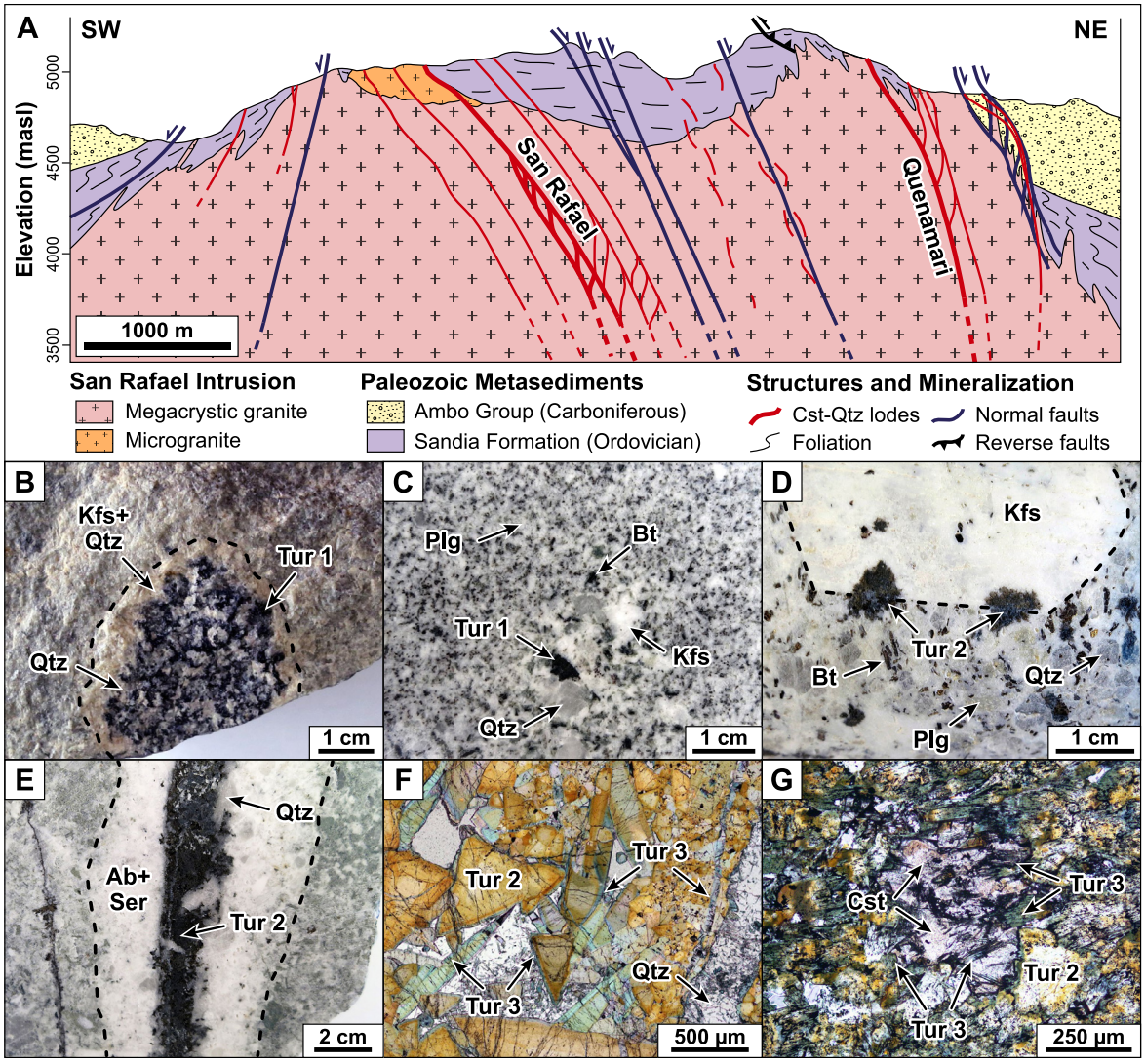


**Fig. 1.** A: Longitudinal cross-section of the San Rafael Sn (–Cu) deposit, Peru. B to G: Petrographic features of the studied tourmaline samples (pictures from Harlaux et al., 2020). B: Late-magmatic quartz-tourmaline nodule (Tur 1) in microgranite. C: Late-magmatic tourmaline (Tur 1) disseminated in microgranite. D: Pre-ore hydrothermal tourmaline (Tur 2) partially replacing a K-feldspar phenocryst in megacrystic granite. E: Pre-ore quartz-tourmaline vein (Tur 2) surrounded by alteration halo crosscutting the megacrystic granite. F: Syn-ore tourmaline (Tur 3) veinlets and overgrowths overprinting a pre-ore quartz-tourmaline vein (Tur 2). G: Syn-ore tourmaline (Tur 3) intergrown with cassiterite. Abbreviations: Ab = albite, Bt = biotite, Cst = cassiterite, Kfs = K-feldspar, Plg = plagioclase, Qtz = quartz, Ser = sericite, Tur = tourmaline. (For interpretation of the colors in the figure(s), the reader is referred to the web version of this article.)

etry (SIMS) in tourmaline from the San Rafael deposit (Peru), one of the world's largest and richest vein-type Sn deposits. Due to its chemical stability and refractory nature, tourmaline is a robust isotopic monitor of ore-forming processes and fluid sources (Slack and Trumbull, 2011; Codeço et al., 2019; Trumbull et al., 2020; Hong et al., 2020). The aim of this study is to use the isotopic composition of tourmaline to trace fluid processes occurring at the magmatic-hydrothermal transition leading to cassiterite deposition. Using quantitative geochemical modeling, we show that in situ $\delta^{18}O$-$\delta^{11}B$ analyses on tourmaline are indicative of fluid exsolution in the early stages of the magmatic-hydrothermal system and, subsequently, mixing with modified meteoric waters triggering cassiterite deposition.

## 2. Geological background

The world-class San Rafael Sn (–Cu) deposit (>1 Mt Sn at average grade of 2%) is located in the northern part of the Central Andean tin belt extending from southeast Peru to Bolivia and northern Argentina. This classic metallogenic province hosts hundreds of Sn-W deposits, which contain widespread tourmaline alteration and high B contents (Lehmann et al., 2000). Mineralization at San Rafael consists of a northwest-trending cassiterite-quartz-chlorite-sulfide vein-breccia system hosted by a late Oligocene (ca. 25 Ma) peraluminous granitic complex and by Ordovician metasediments of the Sandia Formation (Fig. 1A; Kontak and Clark, 2002; Mlynarczyk et al., 2003). The San Rafael deposit is characterized by abundant tourmaline, both of magmatic and hydrothermal origin (Kontak and Clark, 2002; Mlynarczyk and Williams-Jones, 2006). Three major tourmaline (Tur) generations were identified at San Rafael (Harlaux et al., 2020): (i) Tur 1 is found in peraluminous granites as quartz-tourmaline nodules and disseminations (Fig. 1B-C) and is interpreted to be late-magmatic; it is texturally homogeneous and has dravitic composition, close to the schorl-dravite limit, with Fe/(Fe + Mg) ratios of 0.36-0.52; (ii) Tur 2 is pre-ore hydrothermal tourmaline crosscutting the granites and host rocks and formed during post-magmatic alteration and veining (Fig. 1D-E); it shows oscillatory zoning at the microscopic scale and has intermediate compositions ranging from dravite to schorl, with Fe/(Fe + Mg) ratios between 0.01 and 0.83; (iii) Tur 3 is

syn-ore hydrothermal tourmaline forming widespread microscopic veinlets and overgrowths, partly crosscutting the previous tourmaline generations (Fig. 1F-G); it has schorl to foitite compositions, with Fe/(Fe + Mg) = 0.48-0.94, and is locally intergrown with cassiterite and chlorite of the main ore stage. In the present study, we selected representative samples covering the different generations of magmatic to hydrothermal tourmaline (Tur 1 to Tur 3). These samples were mostly collected from underground workings in the San Rafael mine (between 3,610 and 4,475 masl) and were texturally and chemically characterized by Harlaux et al. (2020).

## 3. Analytical methods

### 3.1. Oxygen isotope analysis

Oxygen isotope analyses of tourmaline and quartz were performed at the SwissSIMS ion probe national facility at the University of Lausanne (Switzerland) using a Cameca IMS 1280-HR instrument. A total of 180 $^{18}O/^{16}O$ isotopic ratio analyses were performed on tourmaline and quartz chips placed in indium mounts together with grains of three tourmaline (UNIL-T2, UNIL-T6, and IAEA-B-4; Marger et al., 2019) and one quartz (UNIL-Q1; Seitz et al., 2017) reference materials. The complete SIMS dataset for O isotopes is reported in Supplementary Table S1. Prior to the SIMS session, the mounts were cleaned with dry ethanol and were dried in an oven at 60 °C for 24 h, and then coated with a 35-40 nm-thick layer of gold. Oxygen isotope measurements were done with a 10 kV $Cs^+$ primary beam and a ~2 nA current, resulting in a ~15 µm beam size. $^{16}O$ and $^{18}O$ secondary ions, accelerated at 10 kV, were measured at a mass resolving power M/ΔM of 2400 using an entrance slit open at 122 µm and the multicollection exit slit 1, and were counted in multicollection mode on Faraday cups (L'2 with $10^{11}$ Ω resistor for $^{16}O$ and H'2 with $10^{10}$ Ω resistor for $^{18}O$). The background of the Faraday cups was calibrated at the beginning of each day session, and a nuclear magnetic resonance was used to lock the magnetic field. Each calculated isotopic ratio $^{18}O/^{16}O$ corresponds to 5 measurement blocks of 4 cycles per block, resulting in 20 cycles of acquisition with counting times of 5 s per cycle on both masses simultaneously. Consequently, each analysis takes ~3.5 min, including presputtering (30 s) and automated centering of secondary ions (60 s). All data have been obtained during the same SIMS session in March 2018. The reference materials were measured between every 5 to 8 unknowns for monitoring the instrument stability and analytical accuracy. The average reproducibility on the reference materials was better than 0.4‰ (2SD) and internal error for each analysis lower than 0.2‰ (2SD). After correction of the instrumental mass fractionation (IMF), the measured $^{18}O/^{16}O$ isotopic ratios were corrected for tourmaline matrix effect based on the Mg/(Mg + Fe) and Al(Y) contents determined independently by electron microprobe (Marger et al., 2019; Harlaux et al., 2020). The average IMF for all sessions of O isotope measurement was about 3.6 ± 0.2‰ for IAEA-B4 schorl, 2.3 ± 0.3‰ for UNIL-T2 dravite, 3.6 ± 0.3‰ for UNIL-T6 elbaite, and 5.8 ± 0.1‰ for UNIL-Q1 quartz. The IMF dependence on tourmaline chemistry (between schorl and dravite) is therefore 1.3‰ for O isotopes. Results are reported in $\delta^{18}O = 1000 \times [(^{18}O/^{16}O_{sample})/(^{18}O/^{16}O_{V\text{-}SMOW}) - 1)]$ in ‰ relative to the Vienna Standard Mean Ocean Water (V-SMOW).

### 3.2. Boron isotope analysis

Boron isotope analyses of tourmaline were performed at the SwissSIMS ion probe national facility at the University of Lausanne (Switzerland) using a Cameca IMS 1280-HR instrument. A total of 166 $^{11}B/^{10}B$ isotopic ratio analyses were performed on the same tourmaline chips analyzed for O isotopes. Each indium mount included grains of three tourmaline reference materials (UNIL-T2, UNIL-T6, and IAEA-B-4; Marger et al., 2020). The complete SIMS dataset for B isotopes is reported in Supplementary Table S1. Sample preparation was the same as for O isotope analysis. Boron isotope measurements were done with a 13 kV $O^-$ duoplasmatron primary beam and a ~5-6 nA current, resulting in a ~20 µm beam size. $^{10}B$ and $^{11}B$ secondary ions, accelerated at 10 kV, were measured at a mass resolving power M/ΔM of 2400 (entrance slit at 100 µm and exit slit 1 of the multicollection) and were counted in multicollection mode on Faraday cups (L'2 for $^{10}B$ and H'2 for $^{11}B$, both set with $10^{11}$ Ω resistors). Typical count rate obtained on $^{10}B$ was $2.5 \times 10^6$ cps (count per second) and $9 \times 10^6$ cps for $^{11}B$. The background of the Faraday cups was calibrated at the beginning of each day session, and a nuclear magnetic resonance was used to lock the magnetic field. Each calculated isotopic ratio $^{11}B/^{10}B$ corresponds to 3 measurement blocks of 10 cycles per block, resulting in 30 cycles of acquisition with counting times of 5 s per cycle on each mass. Each analysis takes ~4.5 min, including presputtering (50 s) and automated centering of secondary ions (60 s). This setting allowed an average reproducibility on the reference materials better than 0.6‰ (2SD) and internal error for each analysis lower than 0.4‰ (2SD). All data have been obtained during the same SIMS session in November 2018. The reference materials were measured between every 2 to 4 unknowns for monitoring the instrument stability and analytical accuracy. After correction of the IMF, the measured $^{11}B/^{10}B$ isotopic ratios were corrected for tourmaline matrix effect based on the wt.% FeO + MnO content determined independently by electron microprobe (Marger et al., 2020; Harlaux et al., 2020). The average IMF for all sessions of B isotope measurement was about 20.6 ± 0.7‰ for IAEA-B4 schorl and about 24.1 ± 0.9‰ for UNIL-T2 dravite. The IMF dependence on tourmaline chemistry (between schorl and dravite) is therefore 3.5‰ for B isotopes. Results are reported in $\delta^{11}B = 1000 \times [(^{11}B/^{10}B_{sample})/(^{11}B/^{10}B_{NIST\ SRM\ 951}) - 1]$ in ‰ relative to the NIST SRM 951.

## 4. Results

### 4.1. Oxygen and boron isotopic compositions of tourmaline

The $\delta^{18}O$ and $\delta^{11}B$ compositions of tourmaline measured by SIMS are reported in Supplementary Table S1. Late-magmatic Tur 1 has a near-constant $\delta^{18}O$ isotopic composition falling in a range between 10.6‰ and 11.6‰, whereas its $\delta^{11}B$ composition is more variable ranging between −11.1‰ and −7.8‰ (Fig. 2A). No significant core-rim isotopic zoning is observed. Pre-ore hydrothermal Tur 2 has more variable values of $\delta^{18}O$ of 10.7‰ to 14.1‰ and $\delta^{11}B$ of −11.5‰ to −6.9‰, overlapping with those of Tur 1. In detail, metasediment-hosted Tur 2 shows higher $\delta^{18}O$ values (13.6-14.1‰) than granite-hosted Tur 2 (10.7-11.9‰) while their $\delta^{11}B$ compositions overlap. In a single oscillatory-zoned Tur 2 crystal, isotopic variations of 1.0‰ in $\delta^{18}O$ and 3.5‰ in $\delta^{11}B$ are reached overall from the base of the crystal to the tip (Fig. 3). These variations outline pseudo-periodic cycles at the microscopic scale suggesting a dynamic environment likely caused by repeated fluid pulses. Syn-ore hydrothermal Tur 3 has lighter $\delta^{18}O$ values ranging from 4.9‰ to 10.2‰ and in part heavier $\delta^{11}B$ values from −9.9‰ to −5.4‰. No relation between sample location in the deposit and isotopic composition of tourmaline was found.

### 4.2. Quartz-tourmaline oxygen isotope equilibrium temperatures

The $\delta^{18}O$ compositions of magmatic and hydrothermal quartz showing equilibrium textures with tourmaline were also measured

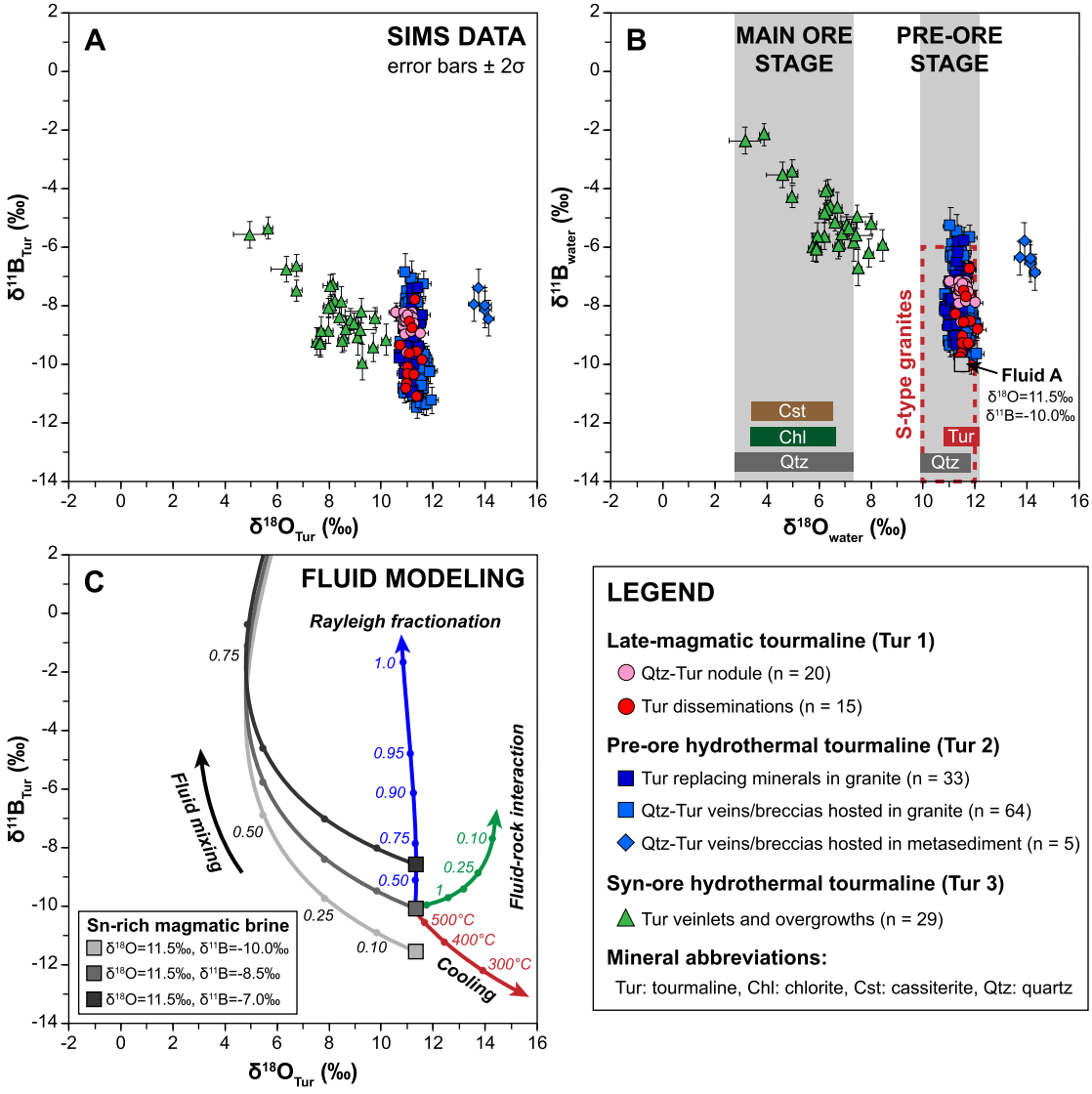


**Fig. 2.** A: Plot of $\delta^{18}O$ vs. $\delta^{11}B$ composition of magmatic and hydrothermal tourmaline (Tur 1 to Tur 3) from the San Rafael deposit determined by secondary ion mass spectrometry (SIMS). B: Calculated $\delta^{18}O$ vs. $\delta^{11}B$ composition of water equilibrated with tourmaline by assuming crystallization temperatures of 650 °C for Tur 1, 550 °C for Tur 2, and 350 °C for Tur 3. The field for S-type granites is from Trumbull and Slack (2018) and Harris et al. (1997). Calculated $\delta^{18}O$ values for water equilibrated with minerals from the pre-ore stage (Qtz, Tur) at 550 °C and the main ore stage (Qtz, Cst, Chl) at 350 °C are shown. C: Modeling of $\delta^{18}O$ vs. $\delta^{11}B$ composition of tourmaline calculated for different fluid evolution scenarios: cooling of a single-phase magmatic fluid (in red), Rayleigh fractionation of a single-phase magmatic fluid (in blue), fluid-rock interaction between magmatic vapor and the host metasediments (in green), and fluid mixing between a Sn-rich magmatic brine and modified meteoric waters (in black and grey). See text for details.

by SIMS in order to determine crystallization temperatures. The analyzed quartz-tourmaline pairs show primary intergrowth textures and lack hydrothermal alteration features, as revealed by preliminary cathodoluminescence quartz imaging. Results of $\delta^{18}O$ compositions of quartz and tourmaline are reported in the Supplementary Table S2 and in Fig. 4. Isotope equilibrium temperatures for quartz-tourmaline pairs were calculated using the equation of Matthews et al. (2003), which is the most appropriate for estimating temperatures in peraluminous granitic systems (Marger et al., 2019). Quartz-tourmaline $\delta^{18}O$ compositions yield equilibrium temperatures of 615 ± 38 °C for Tur 1 and 530 ± 25 °C for Tur 2 (Fig. 4). This indicates temperatures of 500° to 600 °C for the magmatic-hydrothermal transition, which is in agreement with the earliest recorded fluids at San Rafael as revealed by previous fluid inclusion studies on magmatic quartz phenocrysts and pre-ore quartz-tourmaline veins (Kontak and Clark, 2002; Wagner et al., 2009).

## 5. Discussion

### 5.1. Origin and evolution of the boron-rich hydrothermal fluids

The upper values for the quartz-tourmaline isotope thermometer indicate crystallization temperatures of about 650 °C for Tur 1 and 550 °C for Tur 2. No quartz directly intergrown with Tur 3 was found, but previous works reported homogenization temperatures of about 350 °C for primary fluid inclusions hosted in cassiterite (Wagner et al., 2009). Because Tur 3 co-precipitated with cassiterite, an average value of 350 °C is assumed to be the best temperature proxy for its formation. Considering crystallization temperatures of 650 °C for Tur 1, 550 °C for Tur 2, and 350 °C for Tur 3, we calculated the $\delta^{18}O$ and $\delta^{11}B$ composition of water in equilibrium with tourmaline (Fig. 2B) using the O and B isotope fractionation factors of Zheng (1993) and Meyer et al. (2008), respectively. Changing the temperature of tourmaline formation by ± 50 °C would shift the calculated range of water compositions by

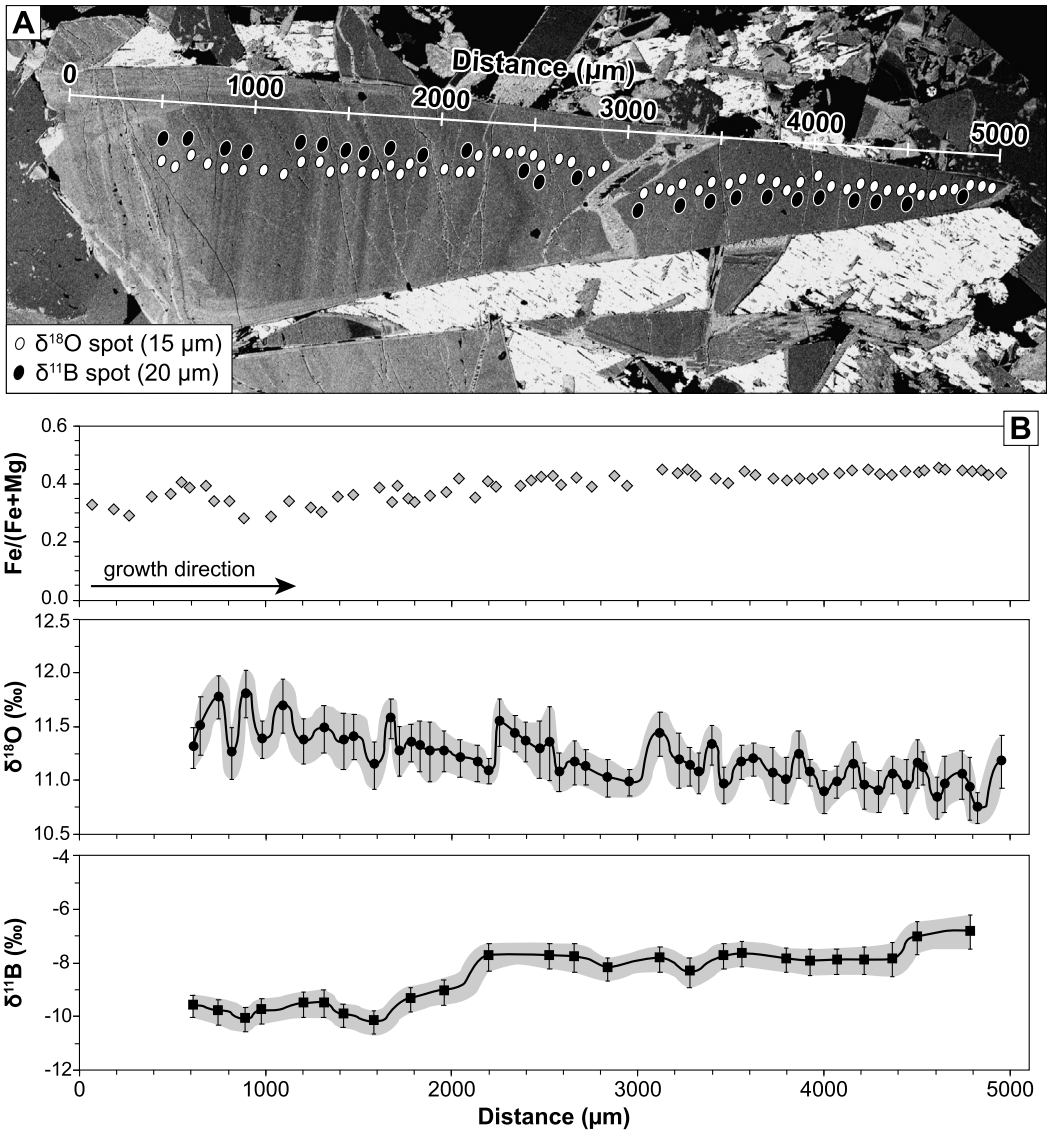


**Fig. 3.** In situ $\delta^{18}O$ and $\delta^{11}B$ variations in a single oscillatory-zoned tourmaline crystal (Tur 2) from a granite-hosted pre-ore quartz-tourmaline vein. A: Backscattered electron (BSE) image of tourmaline showing primary growth zoning. B: $\delta^{18}O$ and $\delta^{11}B$ variations along a transect perpendicular to growth banding (error bars are $2\sigma$). Chemical variations of the Fe/(Fe + Mg) ratio reflect the oscillatory zoning visible on the BSE image (data from Harlaux et al., 2020).

a maximum of ± 1.0‰ in $\delta^{18}O$ and ± 0.5‰ in $\delta^{11}B$. The isotopic compositions of water equilibrated with granite-hosted Tur 1 and Tur 2 overlap over a range of $\delta^{18}O$ values from 10.9‰ to 12.1‰ and $\delta^{11}B$ values from −10.0‰ to −5.3‰. These $\delta^{18}O$ values are consistent with previous bulk $\delta^{18}O$ analyses of quartz and tourmaline separates from the pre-ore stage equilibrated with water at 550 °C (Supplementary Table S3), while the $\delta^{11}B$ values fall in the $\delta^{11}B$ range reported from melt inclusions in Bolivian Sn porphyries (Wittenbrink et al., 2009). The values of $\delta^{18}O = 11.5‰$ and $\delta^{11}B = -10.0‰$ allow defining a single fluid endmember ("fluid A" in Fig. 2B) that fits the typical isotopic compositional range of a magmatic fluid derived from a S-type granite (Harris et al., 1997; Trumbull and Slack, 2018). The magmatic origin of the fluid A is supported by the high-salinity (40-60 wt.% NaCl eq) and high-temperatures (350-550 °C) of primary multiphase aqueous inclusions coexisting with low-salinity vapor inclusions in magmatic quartz phenocrysts and quartz-tourmaline veins at San Rafael, which are interpreted to be formed under lithostatic fluid pressure of 0.8 to 1.0 kbar (Kontak and Clark, 2002; Wagner et al., 2009).

Considering values of $\delta^{18}O = 11.5‰$ and $\delta^{11}B = -10.0‰$ for the magmatic brine and using liquid-vapor isotopic fractionation factors extrapolated to 550 °C (Shmulovich et al., 1999; Liebscher et al., 2005), the coexisting vapor would have $\delta^{18}O = 11.3‰$ and $\delta^{11}B = -8.1‰$. Assuming a 20:80 proportion of liquid (45 wt.% NaCl) and vapor (1 wt.% NaCl), the single-phase magmatic fluid would have an initial salinity of ca. 10 wt.% NaCl and isotopic values of $\delta^{18}O = 11.4‰$ and $\delta^{11}B = -8.5‰$. The increasing trend in $\delta^{11}B$ at near-constant $\delta^{18}O$ values observed for granite-hosted Tur 1 and Tur 2 may therefore reflect the progressive degassing of the silicate melt and phase separation of the single-phase magmatic fluid, similar to what is traditionally observed for H isotope fractionation (Hedenquist and Lowenstern, 1994). The isotopic composition of water in equilibrium with metasediment-hosted Tur 2 differs from their granite-hosted equivalent by higher $\delta^{18}O$ values between 13.7‰ and 14.3‰ while their $\delta^{11}B$ values of −6.8‰ to −5.8‰ overlap. These $\delta^{18}O$-$\delta^{11}B$ compositions are interpreted to represent a fluid endmember with $\delta^{18}O = 14.0‰$ and $\delta^{11}B = -6.0‰$ that possibly corresponds to B-rich magmatic vapor that ascended toward the top of the intrusion upon phase separation and interacted with the host metamorphic rocks, while the mag-

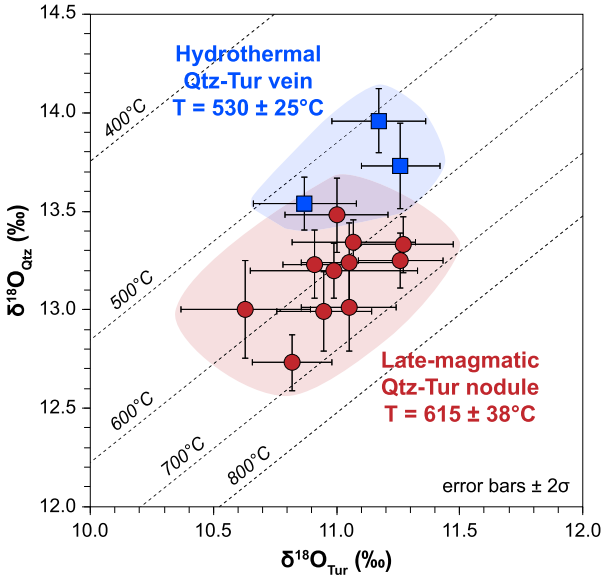


**Fig. 4.** Plot of $\delta^{18}O$ values for quartz (Qtz) and tourmaline (Tur) pairs of magmatic and hydrothermal origin from the San Rafael deposit. Isotherms are plotted using the quartz-tourmaline oxygen isotope fractionation equation of Matthews et al. (2003).

matic brine remained dominantly in the upper part of the granitic stock. The isotopic composition of water equilibrated with Tur 3 plots along an array ranging from $\delta^{18}O = 8.4‰$ and $\delta^{11}B = -6.7‰$ to $\delta^{18}O = 3.2‰$ and $\delta^{11}B = -2.1‰$ (Fig. 2B). This range of $\delta^{18}O$ values covers the previous bulk $\delta^{18}O$ compositions of ore-stage quartz, cassiterite, and chlorite equilibrated with water at 350 °C (Supplementary Table S3). The observed $\delta^{18}O$-$\delta^{11}B$ array suggests a mixing process between a magmatic fluid and another fluid endmember of external origin, having lighter $\delta^{18}O$ and heavier $\delta^{11}B$ composition.

### 5.2. Quantitative modeling of fluid evolution

Based on the tourmaline O and B isotopic compositions, we tested different scenarios considering cooling, Rayleigh fractionation, fluid-rock interaction, and fluid mixing as major processes controlling cassiterite deposition. The calculations are detailed in the Supplementary Material and the results are reported in Supplementary Tables S4 to S9. The calculated $\delta^{18}O$ and $\delta^{11}B$ compositions of tourmaline for each scenario (Fig. 2C) were then compared with the ones measured by SIMS (Fig. 2A). The isotopic composition of Tur 2 was modeled assuming that the starting magmatic fluid is single-phase and has a temperature of 550 °C, a 10 wt.% NaCl salinity, and isotopic values of $\delta^{18}O = 11.4‰$ and $\delta^{11}B = -8.5‰$. Cooling of this magmatic fluid down to 250 °C results in a trend of increasing $\delta^{18}O$ values and decreasing $\delta^{11}B$ values, which does not reproduce the measured isotopic compositions of Tur 2. Rayleigh fractionation driven by tourmaline crystallization from a single-phase magmatic fluid or a magmatic brine ("fluid A"), at decreasing temperatures from 550° to 500 °C, results in a trend of near-constant $\delta^{18}O$ and increase in $\delta^{11}B$ values. This reproduces closely the isotopic compositional range of granite-hosted Tur 2 for 10% to 90% fractionation of the initial magmatic fluid. Fluid-rock interaction between an ascending B-rich magmatic vapor and the host metasediments was modeled for different water/rock ratios (0.1 to 10) at 500 °C by assuming isotopic exchange with muscovite (Zheng, 1993; Wunder et al., 2005), which is the most abundant and the main B-carrier mineral in metasediments from the Sandia Formation. We assumed that the magmatic vapor has a temperature of 500 °C, a 1 wt.% NaCl salinity, and isotopic values of $\delta^{18}O = 11.3‰$ and $\delta^{11}B = -8.1‰$. A concentration of 3,000 ppm B was estimated for the magmatic vapor based on measurements of individual vapor inclusions from granite-related Sn-W deposits (Audétat et al., 2000a,b). For the metasediments, an initial $\delta^{18}O = 14.0‰$ was assumed based on the average O isotopic compositions of Early Paleozoic shales (Bindeman et al., 2016), and values of $\delta^{11}B = -11.0‰$ and B = 150 ppm were taken from average bulk analyses of representative metasediment samples of the Sandia Formation (Supplementary Table S10). Results of the fluid-rock interaction modeling reproduce the measured isotopic compositions of metasediment-hosted Tur 2 for moderate water/rock ratios of 0.1-0.3.

The isotopic composition of Tur 3 was modeled using a fluid mixing scenario between a magmatic brine and modified meteoric waters. For the magmatic brine, we assumed a temperature of 550 °C, $\delta^{18}O = 11.5‰$, and variable $\delta^{11}B$ (−10.0, −8.5, and −7.0‰) in order to cover the range of 3‰ variation in $\delta^{11}B$ observed for Tur 1 to Tur 2 (Fig. 2A). A concentration of 1,500 ppm B was assumed for the magmatic fluid based on measurements of individual brine inclusions from granite-related Sn-W deposits (Audétat et al., 2000a,b; Thomas et al., 2003). In contrast to the pre-ore hydrothermal stage yielding quartz-tourmaline veins and breccias, the salinity of the ore-forming magmatic brine is unknown. Therefore, we considered different initial fluid salinities (45, 35, and 30 wt.% NaCl) for the calculations. Stable isotope measurements of volcanic glasses in the Peruvian Eastern Cordillera yield estimates of $\delta^{18}O = -8.0‰$ and $\delta D = -54‰$ for ancient meteoric waters during the late Oligocene (ca. 25 Ma), i.e., coeval with the formation of the San Rafael deposit (Sundell et al., 2019). Using the B meteoric water line of Rose-Koga et al. (2006), we estimated a $\delta^{11}B = 30.0‰$ for the late Oligocene meteoric fluid in the Peruvian Eastern Cordillera, which falls in the typical values of continental rainwaters (Gaillardet and Lemarchand, 2018). Additionally, we assumed a zero salinity and a B concentration of 0.1 ppm for the meteoric fluid. The composition of late Oligocene meteoric waters ($\delta^{18}O = -8.0‰$, $\delta^{11}B = 30.0‰$, B = 0.1 ppm) after interaction with the Sandia metasediments ($\delta^{18}O = 14.0‰$, $\delta^{11}B = -11.0‰$, B = 150 ppm) was estimated using a model of sequential B extraction and addition to downwelling percolating water (Supplementary Material). At a depth of 4 km (corresponding to a lithostatic pressure of 1 kbar and a temperature of 120 °C), the modified meteoric water after exchange with the metasediments would contain 600 ppm B and would have isotopic values of $\delta^{18}O = -3.3‰$ and $\delta^{11}B = 16.0‰$ for a moderate water/rock ratio of 0.5. The calculated B concentrations and $\delta^{11}B$ values are consistent with measurements of modern geothermal waters from meteoric-dominated hydrothermal systems, such as Larderello in Italy (Duchi et al., 1992; Pennisi et al., 2001). The fluid mixing modeling between a magmatic brine and modified meteoric waters results in a systematic trend of decreasing $\delta^{18}O$ and increasing $\delta^{11}B$, which reproduces the full range of isotopic compositions of Tur 3 for degrees of mixing between 5% and 60% of modified meteoric water. While different initial salinities (45, 35, and 30 wt.% NaCl) of the magmatic brine yield similar mixing curves, the fluid salinity changes the fraction of meteoric water that is required to reproduce the measured $\delta^{18}O$ and $\delta^{11}B$ compositions of Tur 3 (Supplementary Material). Fluid mixing modeling combined with salinity estimates from primary fluid inclusions hosted in ore-stage minerals (12-22 wt.% NaCl eq; Kontak and Clark, 2002; Wagner et al., 2009) indicate that the magmatic brine involved in the precipitation of Tur 3 had a salinity of ca. 30 wt.% NaCl.

### 5.3. Genetic model and tin mineralization

Experimental work showed that high B contents (>1 wt.% $B_2O_3$) in peraluminous granitic melts lower solidus temperatures

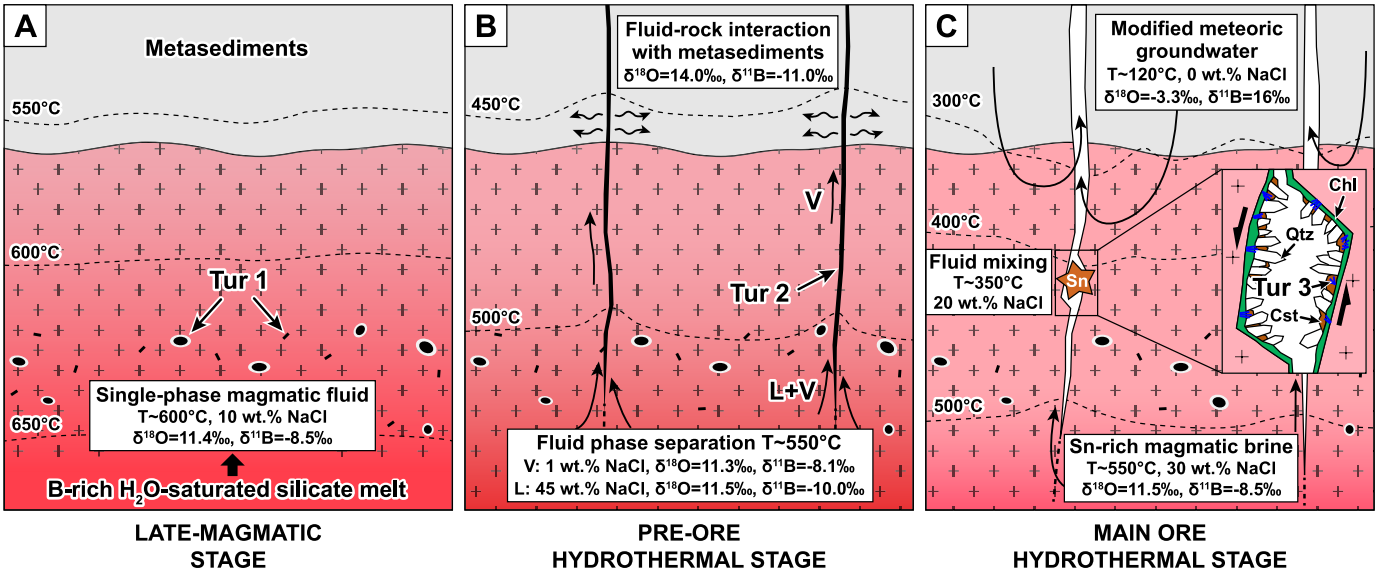


**Fig. 5.** Fluid evolution model for the San Rafael Sn (–Cu) deposit. A: Crystallization of late-magmatic disseminated tourmaline and quartz-tourmaline nodules (Tur 1) was followed by exsolution of a B-rich single-phase magmatic fluid. B: Phase separation of the B-rich single-phase magmatic fluid into low-salinity vapor (V) and high-salinity liquid (L) yielded the formation of pre-ore quartz-tourmaline veins and breccias (Tur 2) cutting the granite and the host metasediments. C: Mixing of a Sn-rich magmatic brine with modified meteoric waters circulating in the upper parts of the granite resulted in the deposition of cassiterite (Cst) together with quartz (Qtz), chlorite (Chl), and syn-ore tourmaline (Tur 3) in veins and breccias.

to <680 °C at 1 kbar, reduce melt viscosity, and increase water solubility (Dingwell et al., 1996). The San Rafael granite is characterized by a moderately fractionated peraluminous composition and whole-rock B content of 60 to 160 ppm (Kontak and Clark, 2002; Mlynarczyk et al., 2003; Harlaux et al., 2020). This implies that the San Rafael silicate melt had initially much higher B contents owing to elevated B fluid/melt partition coefficients in granitic systems (Hervig et al., 2002; Thomas et al., 2003; Schatz et al., 2004; Fiedrich et al., 2020). Crystallization of Tur 1 at ca. 650 °C is interpreted to have occurred during the late-magmatic stage of the San Rafael intrusion prior or concomitantly to the exsolution of a B-rich single-phase magmatic fluid (Fig. 5A). The magmatic-hydrothermal transition occurred between 500° and 600 °C as indicated by temperature estimates from quartz-tourmaline pairs, but the single-phase magmatic fluid likely exsolved at temperatures close to 600 °C. During water exsolution, the immiscible volatile phase preferentially partitions B and becomes isotopically heavier relative to the granitic melt (Maner and London, 2018). This is possibly reflected by the increasing trend in $\delta^{11}$B observed for granite-hosted Tur 1 and Tur 2. The overpressured single-phase magmatic fluid triggered hydrofracturing of the roof of the crystallizing magma chamber resulting in phase separation into vapor (ca. 1 wt.% NaCl) and brine (ca. 45 wt.% NaCl) and the formation of Tur 2 in veins and breccias (Fig. 5B). This likely occurred under dominant lithostatic pressure conditions as reported by previous fluid inclusion studies (Kontak and Clark, 2002; Wagner et al., 2009). Phase separation also resulted in geochemical decoupling, where Sn preferentially partitions into the brine whereas B partitions into the vapor (Heinrich et al., 1999; Audétat et al., 2000a,b; Schatz et al., 2004; Foustoukos and Seyfried, 2007; Fiedrich et al., 2020). Based on their similar $\delta^{18}$O-$\delta^{11}$B values, we interpret that Tur 1 and Tur 2 crystallized in a continuously evolving magmatic-hydrothermal system in which isotopic variations were dominantly driven by Rayleigh fractionation.

The $\delta^{18}$O-$\delta^{11}$B array observed for Tur 3 reflects infiltration of modified meteoric waters into the hydrothermal system during the main ore stage. Most likely, this occurred during a transition from lithostatic to hydrostatic pressure conditions caused by the opening of dilatational fault jogs during sinistral-normal strike-slip faulting (Mlynarczyk et al., 2003; Wagner et al., 2009). This process caused the mixing and the cooling of a hot Sn-rich magmatic brine (ca. 30 wt.% NaCl) with modified meteoric waters (Fig. 5C), resulting in destabilization of Sn-chloride complexes and the consecutive precipitation of cassiterite (Schmidt, 2018). This interpretation is consistent with the evolution of the San Rafael magmatic-hydrothermal system from reducing toward relatively more oxidizing conditions as deduced from the changing textural and compositional features of Tur 1 to Tur 3 (Harlaux et al., 2020). The Sn-rich magmatic brine was produced during a new hydrothermal activity in the magma reservoir. We propose that this occurred either during the fluid exsolution from an underlying residual granitic magma, or during the mixing of a residual brine from the pre-ore stage, temporally stored at depth, with a new pulse of low-salinity magmatic fluid, as proposed for other ore deposits (Kouzmanov et al., 2010; Rottier et al., 2018).

## 6. Conclusions

High-resolution in situ $\delta^{18}$O-$\delta^{11}$B analysis of tourmaline has allowed tracing the fluid evolution of the San Rafael magmatic-hydrothermal system. Our results show that late-magmatic Tur 1 and pre-ore hydrothermal Tur 2 formed in a continuously evolving magmatic-hydrothermal system, whereas syn-ore hydrothermal Tur 3 records variable degrees of mixing between Sn-rich magmatic brine and modified meteoric waters. Fluid mixing related to lithostatic-hydrostatic pressure transition and infiltration of meteoric waters into the hydrothermal system was the key mechanism triggering cassiterite deposition in the San Rafael Sn (–Cu) deposit. Furthermore, this study demonstrates that the combination of in situ $\delta^{18}$O and $\delta^{11}$B analyses of tourmaline is a powerful approach for understanding fluid processes in dynamic magmatic-hydrothermal environments.

## CRediT authorship contribution statement

**Matthieu Harlaux:** Writing - original draft preparation, Review and editing, Data acquisition and treatment, Data analysis and interpretation. **Kalin Kouzmanov:** Review and editing, Data analysis and interpretation, Supervision, Conceptualization. **Stefano Gialli:** Review and editing. **Katharina Marger:** Review and editing, Data

acquisition and treatment. **Anne-Sophie Bouvier:** Review and editing, Data acquisition and treatment. **Lukas Baumgartner:** Review and editing, Data acquisition and treatment. **Andrea Rielli:** Review and editing, Data acquisition and treatment. **Andrea Dini:** Review and editing, Data acquisition and treatment, Data analysis and interpretation. **Alain Chauvet:** Review and editing. **Miroslav Kalinaj:** Review and editing, Conceptualization. **Lluís Fontboté:** Review and editing, Data analysis and interpretation, Supervision, Conceptualization.

## Declaration of competing interest

The authors declare that they have no known competing financial interests or personal relationships that could have appeared to influence the work reported in this paper.

## Acknowledgements

This research was supported by the Swiss National Science Foundation (grant SNSF S19053_169901) and the company Minsur S.A. The authors thank Drs. Michel Pichavant and David Dolejš for fruitful discussions during this project. We are also grateful to Drs. Robert Trumbull and Fernando Tornos for their constructive and thorough reviews, which helped to improve the original manuscript. Dr. Rosemary Hickey-Vargas is thanked for the editorial handling.

## Appendix A. Supplementary material

## References

Audétat, A., Günther, D., Heinrich, C.A., 2000a. Causes for large-scale metal zonation around mineralized plutons: fluid inclusion LA-ICP-MS evidence from the Mole Granite, Australia. Econ. Geol. 95, 1563–1581.

Audétat, A., Günther, D., Heinrich, C.A., 2000b. Magmatic-hydrothermal evolution in a fractionating granite: a microchemical study of the Sn-W-F-mineralized Mole Granite (Australia). Geochim. Cosmochim. Acta 64, 3373–3393.

Bindeman, I.N., Bekker, A., Zakharov, D.O., 2016. Oxygen isotope perspective on crustal evolution on early Earth: a record of Precambrian shales with emphasis on Paleoproterozoic glaciations and Great Oxygenation Event. Earth Planet. Sci. Lett. 437, 101–113.

Černý, P., Blevin, P.L., Cuney, M., London, D., 2005. Granite-related ore deposits. In: Hedenquist, J.W., Thompson, J.F.H., Goldfarb, R.J., Richards, J.P. (Eds.), 100th Anniversary. In: Economic Geology, 100th Anniversary Volume 1905–2005, pp. 337–370.

Codeço, M.S., Weis, P., Trumbull, R.B., Glodny, J., Wiedenbeck, M., Romer, R.L., 2019. Boron isotope muscovite-tourmaline geothermometry indicates fluid cooling during magmatic-hydrothermal W-Sn ore formation. Econ. Geol. 114, 153–163.

Dingwell, D.B., Pichavant, M., Holtz, F., 1996. Experimental studies of boron in granitic melts. In: Grew, E.S., Anovitz, L. (Eds.), Boron: Mineralogy, Petrology, and Geochemistry in the Earth's Crust. In: Mineralogical Society of America, Reviews in Mineralogy, vol. 33, pp. 331–385.

Duchi, V., Minissale, A., Manganelli, M., 1992. Chemical composition of natural deep and shallow hydrothermal fluids in the Larderello geothermal field. J. Volcanol. Geotherm. Res. 49, 313–328.

Fekete, S., Weis, P., Driesner, T., Bouvier, A.S., Baumgartner, L., Heinrich, C.A., 2016. Contrasting hydrological processes of meteoric water incursion during magmatic–hydrothermal ore deposition: an oxygen isotope study by ion microprobe. Earth Planet. Sci. Lett. 451, 263–271.

Fiedrich, A.M., Laurent, O., Heinrich, C.A., Bachmann, O., 2020. Melt and fluid evolution in an upper-crustal magma reservoir, preserved by inclusions in juvenile clasts from the Kos Plateau Tuff, Aegean Arc, Greece. Geochim. Cosmochim. Acta 280, 237–262.

Foustoukos, D.I., Seyfried Jr, W.E., 2007. Trace element partitioning between vapor, brine and halite under extreme phase separation conditions. Geochim. Cosmochim. Acta 71, 2056–2071.

Gaillardet, J., Lemarchand, D., 2018. Boron in the weathering environment. In: Marschall, H.R., Foster, G.L. (Eds.), Boron Isotopes - The Fifth Element, Advances in Isotope Geochemistry. Springer-Verlag, pp. 163–188.

Harlaux, M., Mercadier, J., Marignac, C., Peiffert, C., Cloquet, C., Cuney, M., 2018. Tracing metal sources in peribatholitic hydrothermal W deposits based on the chemical composition of wolframite: the example of the Variscan French Massif Central. Chem. Geol. 479, 58–85.

Harlaux, M., Kouzmanov, K., Gialli, S., Laurent, O., Rielli, O., Dini, A., Chauvet, A., Menzies, A., Kalinaj, M., Fontboté, L., 2020. Tourmaline as a tracer of late-magmatic to hydrothermal fluid evolution: the world-class San Rafael tin (-copper) deposit, Peru. Econ. Geol. 115, 1665–1697.

Harris, C., Faure, K., Diamond, R.E., Scheepers, R., 1997. Oxygen and hydrogen isotope geochemistry of S- and I-type granitoids: the Cape Granite suite, South Africa. Chem. Geol. 143, 95–114.

Hedenquist, J.W., Lowenstern, J.B., 1994. The role of magmas in the formation of hydrothermal ore deposits. Nature 370, 519–527.

Heinrich, C.A., 1990. The chemistry of hydrothermal tin (-tungsten) ore deposition. Econ. Geol. 85, 457–481.

Heinrich, C.A., Günther, D., Audétat, A., Ulrich, T., Frischknecht, R., 1999. Metal fractionation between magmatic brine and vapor, determined by microanalysis of fluid inclusions. Geology 27, 755–758.

Hervig, R.L., Moore, G.M., Williams, L.B., Peacock, S.M., Holloway, J.R., Roggensack, K., 2002. Isotopic and elemental partitioning of boron between hydrous fluid and silicate melt. Am. Mineral. 87, 769–774.

Hong, W., Fox, N., Cooke, D.R., Zhang, L., Fayek, M., 2020. B- and O-isotopic compositions of tourmaline constrain late-stage magmatic volatile exsolution in Tasmanian tin-related granite systems. Miner. Depos. 55, 63–78.

Hulsbosch, N., Boiron, M.C., Dewaele, S., Muchez, P., 2016. Fluid fractionation of tungsten during granite–pegmatite differentiation and the metal source of peribatholitic W quartz veins: evidence from the Karagwe-Ankole Belt (Rwanda). Geochim. Cosmochim. Acta 175, 299–318.

Kontak, D.J., Clark, A.H., 2002. Genesis of the giant, bonanza San Rafael lode tin deposit, Peru: origin and significance of pervasive alteration. Econ. Geol. 97, 1741–1777.

Korges, M., Weis, P., Lüders, V., Laurent, O., 2018. Depressurization and boiling of a single magmatic fluid as a mechanism for tin-tungsten deposit formation. Geology 46, 75–78.

Kouzmanov, K., Pettke, T., Heinrich, C.A., 2010. Direct analysis of ore-precipitating fluids: combined IR microscopy and LA-ICP-MS study of fluid inclusions in opaque ore minerals. Econ. Geol. 105, 351–373.

Legros, H., Richard, A., Tarantola, A., Kouzmanov, K., Mercadier, J., Vennemann, T., Marignac, C., Cuney, M., Wang, R.C., Charles, N., Bailly, L., Lespinasse, M.Y., 2019. Multiple fluids involved in granite-related W-Sn deposits from the world-class Jiangxi province (China). Chem. Geol. 508, 92–115.

Lehmann, B., Dietrich, A., Heinhorst, J., Métrich, N., Mosbah, M., Palacios, C., Schneider, H.-J., Wallianos, A., Webster, J., Winkelmann, L., 2000. Boron in the Bolivian tin belt. Miner. Depos. 35, 223–232.

Liebscher, A., Meixner, A., Romer, R.L., Heinrich, W., 2005. Liquid-vapor fractionation of boron and boron isotopes: experimental calibration at 400 °C/23 MPa to 450 °C/42 MPa. Geochim. Cosmochim. Acta 69, 5693–5704.

Maner, J.L., London, D., 2018. Fractionation of the isotopes of boron between granitic melt and aqueous solution at 700 °C and 800 °C (200 MPa). Chem. Geol. 489, 16–27.

Marger, K., Luisier, C., Baumgartner, L.P., Putlitz, B., Dutrow, B.L., Bouvier, A.-S., Dini, A., 2019. Origin of Monte Rosa whiteschist from in-situ tourmaline and quartz oxygen isotope analysis by SIMS using new tourmaline reference materials. Am. Mineral. 104, 1503–1520.

Marger, K., Harlaux, M., Rielli, A., Baumgartner, L.P., Dini, A., Dutrow, B., Bouvier, A.-S., 2020. Development and re-evaluation of tourmaline reference materials for in situ measurement of boron $\delta$ values by secondary ion mass spectrometry. Geostand. Geoanal. Res. 44, 593–615.

Matthews, A., Putlitz, B., Hamiel, Y., Hervig, R.L., 2003. Volatile transport during the crystallization of anatectic melts: oxygen, boron and hydrogen stable isotope study on the metamorphic complex of Naxos, Greece. Geochim. Cosmochim. Acta 67, 3145–3163.

Meyer, C., Wunder, B., Meixner, A., Romer, R.L., Heinrich, W., 2008. Boron-isotope fractionation between tourmaline and fluid: an experimental re-investigation. Contrib. Mineral. Petrol. 156, 259–267.

Mlynarczyk, M.S., Williams-Jones, A.E., 2006. Zoned tourmaline associated with cassiterite: implications for fluid evolution and tin mineralization in the San Rafael Sn–Cu deposit, southeastern Peru. Can. Mineral. 44, 347–365.

Mlynarczyk, M.S., Sherlock, R.L., Williams-Jones, A.E., 2003. San Rafael, Peru: geology and structure of the worlds richest tin lode. Miner. Depos. 38, 555–567.

Pennisi, M., Magro, G., Adorni-Braccesi, A., Scandiffio, G., 2001. Boron and helium isotopes in geothermal fluids from Larderello (Italy). In: Proceedings of the International Symposium on Water-Rock Interaction 2001. Villasimius, Italy, June 10–15, 2001, pp. 899–902.

Romer, R.L., Kroner, U., 2016. Phanerozoic tin and tungsten mineralization—tectonic controls on the distribution of enriched protoliths and heat sources for crustal melting. Gondwana Res. 31, 60–95.

Rose-Koga, E.F., Sheppard, S.M.F., Chaussidon, M., Carignan, J., 2006. Boron isotopic composition of atmospheric precipitations and liquid–vapour fractionations. Geochim. Cosmochim. Acta 70, 1603–1615.

Rottier, B., Kouzmanov, K., Casanova, V., Wälle, M., Fontboté, L., 2018. Cyclic dilution of magmatic metal-rich hypersaline fluids by magmatic low-salinity fluid: a major process generating the giant epithermal polymetallic deposit of Cerro de Pasco, Peru. Econ. Geol. 113, 825–856.

Schatz, O.J., Dolejš, D., Stix, J., Williams-Jones, A.E., Layne, G.D., 2004. Partitioning of boron among melt, brine and vapor in the system haplogranite–$H_2O$–NaCl at 800 °C and 100 MPa. Chem. Geol. 210, 135–147.

Schmidt, C., 2018. Formation of hydrothermal tin deposits: Raman spectroscopic evidence for an important role of aqueous Sn (IV) species. Geochim. Cosmochim. Acta 220, 499–511.

Seitz, S., Baumgartner, L.P., Bouvier, A.S., Putlitz, B., Vennemann, T., 2017. Quartz reference materials for oxygen isotope analysis by SIMS. Geostand. Geoanal. Res. 41, 69–75.

Shmulovich, K.I., Landwehr, D., Simon, K., Heinrich, W., 1999. Stable isotope fractionation between liquid and vapour in water–salt systems up to 600 °C. Chem. Geol. 157, 343–354.

Slack, J.F., Trumbull, R.B., 2011. Tourmaline as a recorder of ore-forming processes. Elements 7, 321–326.

Sundell, K.E., Saylor, J.E., Lapen, T.J., Horton, B.K., 2019. Implications of variable late Cenozoic surface uplift across the Peruvian central Andes. Sci. Rep. 9, 1–12.

Thomas, R., Förster, H.J., Heinrich, W., 2003. The behaviour of boron in a peraluminous granite-pegmatite system and associated hydrothermal solutions: a melt and fluid-inclusion study. Contrib. Mineral. Petrol. 144, 457–472.

Trumbull, R.B., Slack, J.F., 2018. Boron isotopes in the continental crust: granites, pegmatites, felsic volcanic rocks, and related ore deposits. In: Marschall, H.R., Foster, G.L. (Eds.), Boron Isotopes - The Fifth Element, Advances in Isotope Geochemistry. Springer-Verlag, pp. 249–272.

Trumbull, R.B., Codeço, M.S., Jiang, S.Y., Palmer, M.R., Slack, J.F., 2020. Boron isotope variations in tourmaline from hydrothermal ore deposits: a review of controlling factors and insights for mineralizing systems. Ore Geol. Rev. 125, 103682.

Vallance, J., Cathelineau, M., Marignac, C., Boiron, M.C., Fourcade, S., Martineau, F., Fabre, C., 2001. Microfracturing and fluid mixing in granites: W–(Sn) ore deposition at Vaulry (NW French Massif Central). Tectonophysics 336, 43–61.

Van Daele, J., Hulsbosch, N., Dewaele, S., Boiron, M.C., Piessens, K., Boyce, A., Muchez, P., 2018. Mixing of magmatic-hydrothermal and metamorphic fluids and the origin of peribatholitic Sn vein-type deposits in Rwanda. Ore Geol. Rev. 101, 481–501.

Wagner, T., Mlynarczyk, M.S., Williams-Jones, A.E., Boyce, A.J., 2009. Stable isotope constraints on ore formation at the San Rafael tin-copper deposit, Southeast Peru. Econ. Geol. 104, 223–248.

Wittenbrink, J., Lehmann, B., Wiedenbeck, M., Wallianos, A., Dietrich, A., Palacios, C., 2009. Boron isotope composition of melt inclusions from porphyry systems of the Central Andes: a reconnaissance study. Terra Nova 21, 111–118.

Wunder, B., Meixner, A., Romer, R.L., Wirth, R., Heinrich, W., 2005. The geochemical cycle of boron: constraints from boron isotope partitioning experiments between mica and fluid. Lithos 84, 206–216.

Zheng, Y.-F., 1993. Calculation of oxygen isotope fractionation in hydroxyl-bearing silicates. Earth Planet. Sci. Lett. 120, 247–263.